Journal of Biomedical Optics

BiomedicalOptics.SPIEDigitalLibrary.org

Optical coherence tomography angiography offers comprehensive evaluation of skin optical clearing *in vivo* by quantifying optical properties and blood flow imaging simultaneously

Li Guo
Rui Shi
Chao Zhang
Dan Zhu
Zhihua Ding
Peng Li

SPIE.

Optical coherence tomography angiography offers comprehensive evaluation of skin optical clearing *in vivo* by quantifying optical properties and blood flow imaging simultaneously

Li Guo,[a,†] Rui Shi,[b,c,†] Chao Zhang,[b,c] Dan Zhu,[b,c] Zhihua Ding,[a] and Peng Li[a,*]
[a]Zhejiang University, College of Optical Science and Engineering, State Key Lab of Modern Optical Instrumentation, 38 Zheda Road, Hangzhou, Zhejiang 310027, China
[b]Huazhong University of Science and Technology, Britton Chance Center for Biomedical Photonics, Wuhan National Laboratory for Optoelectronics, 1037 Luoyu Road, Wuhan, Hubei 430074, China
[c]Huazhong University of Science and Technology, Department of Biomedical Engineering, MoE Key Laboratory for Biomedical Photonics, Department of Biomedical Engineering, 1037 Luoyu Road, Wuhan, Hubei 430074, China

Abstract. Tissue optical clearing (TOC) is helpful for reducing scattering and enhancing the penetration depth of light, and shows promising potential in optimizing optical imaging performances. A mixture of fructose with PEG-400 and thiazone (FPT) is used as an optical clearing agent in mouse dorsal skin and evaluated with OCT angiography (Angio-OCT) by quantifying optical properties and blood flow imaging simultaneously. It is observed that FPT leads to an improved imaging performance for the deeper tissues. The imaging performance improvement is most likely caused by the FPT-induced dehydration of skin, and the reduction of scattering coefficient (more than ~40.5%) and refractive-index mismatching (more than ~25.3%) in the superficial (epidermal, dermal, and hypodermal) layers. A high correlation (up to ~90%) between the relative changes in refractive-index mismatching and Angio-OCT signal strength is measured. The optical clearing rate is $\sim 5.83 \times 10^{-5}$ cm/s. In addition, Angio-OCT demonstrates enhanced performance in imaging cutaneous hemodynamics with satisfactory spatiotemporal resolution and contrast when combined with TOC, which exhibits a powerful practical application in studying microcirculation. [DOI: 10.1117/1.JBO.21.8.081202]

Keywords: optical coherence tomography; optical clearing; skin; tissue optical property.

Paper 150796SSR received Nov. 30, 2015; accepted for publication Dec. 31, 2015; published online Mar. 7, 2016.

1 Introduction

Mainly due to high spatial or temporal resolution, optical imaging techniques have been attractive tools in biomedicine with widespread research and clinical applications when compared with nonoptical methods.[1] However, mainly due to the strong scattering in most nontransparent tissues, the strength of the probe light beam attenuates gradually as it penetrates deeper into the tissue. The attenuation effect fundamentally limits the available imaging performances in penetration depth, image contrast, and image resolution.[2–4] In particular, cutaneous blood perfusion is highly correlated to a number of peripheral vascular diseases, but the optical imaging of cutaneous blood vessels is quite challenging due to the high scattering property of skin. By matching the refractive index between different tissue components, tissue optical clearing has been found useful for reducing light scattering and improving imaging performance in a wide range of optical techniques, such as laser speckle contrast imaging (LSCI),[5,6] optical coherence tomography (OCT),[7,8] photoacoustic microscopy,[9,10] confocal microscopy,[11,12] two-photon microscopy,[13,14] and flow cytometry.[15]

Extensive efforts have been devoted to the screening of high-efficiency and biocompatible optical clearing agents (OCAs) or chemical penetration enhancers for improving the diffusion of OCAs within tissues.[3,4] In a previous study, we found a mixture of fructose with PEG-400 and thiazone (FPT) allows *in vivo* blood flow imaging with higher contrast and resolution.[16] Currently, evaluation of a newly developed OCA is usually performed by imaging the blood flow *in vivo*[5,16] or by measuring the optical properties via integration sphere,[17] diffuse reflectance spectroscopy,[18] and OCT[7,19–21] separately. LSCI allows a full-field imaging of the cutaneous blood flow using speckle dynamics and has been used for evaluating the OCA-induced improvement in both the contrast and resolution of blood flow imaging. Due to its lack of depth-resolved information, LSCI fails to measure the optical properties *in vivo*.[22–25] Spectral domain OCT (SDOCT) is capable of high-resolution, real-time, and three-dimensional (3-D) imaging of internal structure of biological tissues in a depth-resolved manner, and the contrast of OCT structure mainly originates from the endogenous differences in optical scattering, eliminating the requirement of tissue-labeling or contrast-enhancing agents.[7,19,21,26] The depth-resolved OCT signal offers an approach for measuring optical properties.[7,19–21] Thus, the attenuation coefficient, refractive-index mismatching extent, and permeation rate of different tissue compounds can be quantified, which has played a vital role in evaluating the changes of tissue optical properties in previous studies.[21] OCA processing, skin optical properties, and blood flow imaging performances are closely correlated, but

*Address all correspondence to: Peng Li, E-mail: peng_li@zju.edu.cn

†These authors contributed equally to this work.

their relationship has seldom been reported. An approach capable of monitoring the agent-induced changes in skin optical properties and flow imaging performance simultaneously is desirable for a comprehensive understanding of a newly developed OCA.

OCT angiography (Angio-OCT) is able to generate structural and angiographic images of skin in parallel. By mathematically analyzing the temporal dynamics of light scattering, Angio-OCT is capable of contrasting the dynamic blood flow against the static tissue bed,[27–32] and enables a label-free, motion-contrast 3-D microangiography. Thus, Angio-OCT is quite suitable for OCA characterization by measuring skin optical properties and evaluating blood flow imaging simultaneously.

Angio-OCT is used in this study for FPT evaluation. The optical clearing efficacy is quantified by calculating the total attenuation coefficient, refractive-index mismatching extent, and permeation rate. FPT-induced improvement in Angio-OCT imaging performance is presented through imaging resolution, contrast, and imaging depth. Further data analysis is performed to evaluate the correlation between the relative changes in Angio-OCT imaging performance and skin optical properties *in vivo*. Finally, since the FPT treatment enables the visualization of deep cutaneous blood vessels, dynamic study of flow response to vasoactive drugs is demonstrated by Angio-OCT.

2 Materials and Methods

2.1 *System Setup*

Angio-OCT is home-built based on a typical SDOCT configuration, as shown in Fig. 1. Briefly, the light source is a broadband superluminescent diode (SLD; Superlum, Carrigtwohill, Ireland, Broadlighters D855-HP2) with a central wavelength of 850 nm and a full-width-half-maximum bandwidth of 100 nm, theoretically offering a high axial resolution of ~3.2 μm in air. An objective lens with a focal length of 40 mm was used to focus the probing light beam on the region of interest, yielding a measured lateral-resolution of ~15 μm. The OCT detection unit in our system was a high-speed spectrometer, equipped with a fast line-scan CMOS camera (Basler, Ahrensburg, Germany, Sprint spL4096-140k) providing a 120-kHz line-scan rate and 2048 active pixels. The spectrometer had a designed spectral resolution of 0.062 nm, providing an imaging range of ~2.9 mm on each side of the zero-delay line in air. The system sensitivity was measured at ~100 dB at the depth position of 0.5 mm, with an incident optical power of 2 mW upon the sample surface.

2.2 *Chemical Agents*

FPT was used in this study for optical clearing. As described in our previous study,[16] FPT was a mixture of saturated fructose (Sinopharm Chemical Reagent Co., Ltd.) solution (78%, w/w) with PEG-400 (Kemiou Reagent Development Corporation) and thiazone (Heming Trading Company Limited) at a volume ratio of 11 : 8 : 1. FPT has a refractive index of 1.4801 and a pH value of 6.0. Norepinephrine (NE), purchased from Affiliated Hospital of Huazhong University of Science and Technology (Wuhan, PRC), was used for the dynamic study of cutaneous blood flow.

2.3 *Animal Preparations*

Male *Balb/c* mice ($N = 15$, 8 weeks old) were obtained from Shanghai Animal Experimental Center (Shanghai, PRC) and fed under specific pathogen-free conditions. Mice were anesthetized by intraperitoneal injection of a mixture of 10% urethane and 2% α-chloralose with a dosage of 0.8 ml/100 g. The dorsal hair was shaved and the residual hair was thoroughly removed with depilatory cream. Then mice were placed on the experimental platform for OCT imaging. All procedures in the experiments were carried out with the guidelines of the Institutional Animal Care and Use Committee of Zhejiang

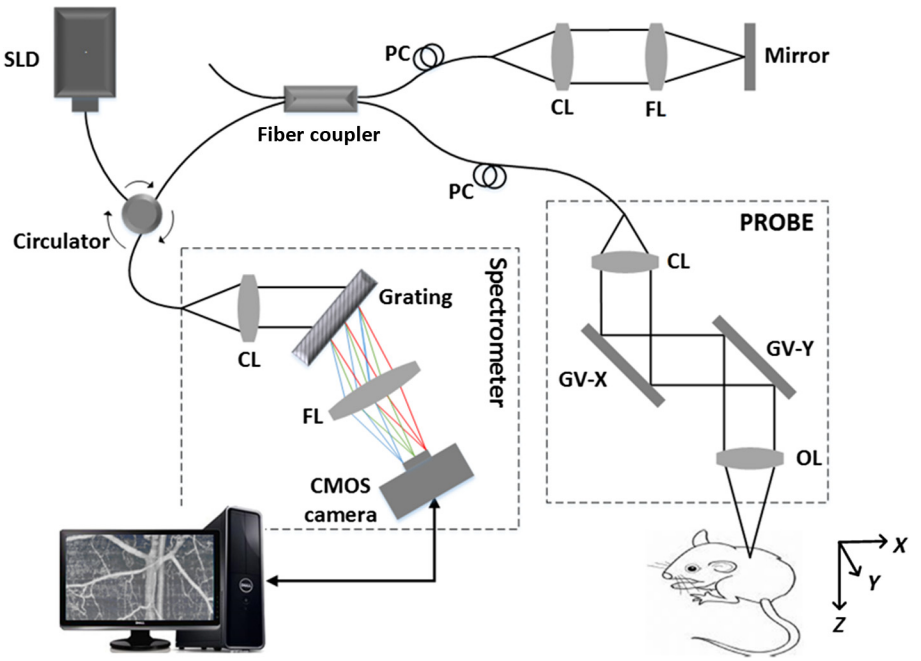

Fig. 1 Schematic of the imaging system used to collect the 3-D spectral interferogram cube for OCT angiography. SLD, super luminescent diode; PC, polarization controller; CL, collimating lens; FL, focusing lens; OL, objective lens.

University, PRC. To evaluate the clearing efficacy of the FPT agent *in vivo*, the dorsal skin of 15 prepared mice was imaged with Angio-OCT before and after topical application of OCAs. Then six of these mice were injected with 100 μl of NE (0.2 μg/μl) after skin became transparent, and the dynamic response of blood flow to the vasoactive drug was monitored for 25 min with a time interval of 1 min.

2.4 *Quantification of Imaging Performance and Skin Optical Properties*

OCT provides depth-resolved images of tissue. Due to the optical scattering and absorption of tissues, the OCT probe light is attenuated as the beam penetrates deeper into the tissue. The OCT depth profile reveals the depth-dependent attenuation coefficient in the tissue. According to Lambert–Beer's law, the OCT depth profile is related to the attenuation coefficient μ_t of tissues as[21,33]

$$\ln\left[\frac{I(z)}{I_0}\right] = -2\mu_t z = -2(\mu_a + \mu_s)z, \tag{1}$$

where I_0 and $I(z)$ are the detected OCT signal intensity at a reference layer and a certain depth z relative to that layer of the tissue, respectively. μ_s and μ_a refer to the scattering and absorption coefficients, respectively. Here, the factor 2 is due to the light propagating through the tissue twice. The attenuation coefficients can be extracted by fitting an exponential curve to the scattering signal. However, this approach requires accurate segmentation of different skin layers, and it is difficult to provide depth-resolved attenuation coefficients. Recently, Vermeer et al.[34] proposed a new method for local attenuation coefficient estimation, which can be expressed as

$$\mu_t[i] \approx \frac{I[i]}{2\Delta \sum_{i+1}^{\infty} I[i]}, \tag{2}$$

where $\mu_t[i]$ and $I[i]$ refer to the attenuation coefficient and signal intensity for the i'th pixel of the OCT image, respectively, and Δ is the pixel size.

The scattering coefficient of tissue is closely dependent on the refractive-index mismatching extent between extracellular fluid (n_{ECF}) and tissue components (e.g., collagen, fibers, and cell) (n_s). In a simple model of scattering dielectric sphere, μ_s can be approximated as[35]

$$\mu_s = \frac{3.28\pi r^2 \rho_s}{1-g}\left(\frac{2\pi r}{\lambda}\right)^{0.37}(m-1)^{2.09}, \tag{3}$$

where ρ_s, r, g, and λ are the volume density of the spheres, the dielectric spherical radius, the scattering anisotropy factor, and the wavelength of the incident light, respectively. $m = (n_s/n_{ECF})$, quantifying the refractive-index mismatching extent between extracellular fluid and tissue components. Given that $\mu_s \gg \mu_a$ in the near-infrared spectral band, we have $\mu_s \approx \mu_t$, and with the reasonable supposition that the changes of ρ_s, r, and g are negligible during the optical clearing process, the OCA-induced relative changes of refractive-index mismatching extent can be evaluated using Eqs. (2) and (3).

In addition, the permeability rate (P) is an important parameter for the evaluation of efficiency of OCAs, which can be estimated by dividing the thickness z_{region} of the region that OCAs reach by the time t_{region} of molecular permeation in the monitored region[21]

$$P = z_{region}/t_{region}. \tag{4}$$

The correlation between the relative changes in refractive-index mismatching $(m-1)$ and Angio-OCT signal strength I can be calculated as

$$R^2 = \frac{\sum_z [I(z)-\bar{I}][M(z)-\bar{M}]}{\sqrt{\sum_z [I(z)-\bar{I}]^2}\sqrt{\sum_z [M(z)-\bar{M}]^2}}, \tag{5}$$

where $I(Z)$ and $M(Z)$ refer to the signal strength I and refractive index mismatching $(m-1)$ at the depth of z, respectively, $\bar{I}$ and $\bar{M}$ are the corresponding average values along the depth.

3 Results

3.1 *Optical Coherence Tomography Structural and Flow Imaging of Mouse Dorsal Skin*

Figure 2 shows the representative OCT structural and angiographic images of mouse dorsal skin *in vivo*. Figure 2(a) is a cross-sectional schematic of the layered skin. Figures 2(b1) and 2(c1) show the representative OCT structural cross-sections before and after the topical application of the FPT agent, respectively. The layered structures of skin are quite vague and difficult to distinguish in Fig. 2(b1). In contrast, the imaging contrast and depth are improved greatly in Fig. 2(c1), and the layered structures and features are clearly identified and manually depicted, including the epidermis (ED), dermis (D), hypodermis (HD), and muscles (M), according to cutaneous anatomical features and the obvious boundaries in the Angio-OCT structural cross-section. The ED-D and HD-M boundaries are visualized clearly, and the dermis exhibits a decreased OCT scattering intensity. The hypodermis appears to be an interwoven structure that is correlated to the adipose cells in the layer. The muscle has a sandwich structure. After the topical application of the FPT agent, the thickness of the epidermis and dermis decreases obviously due to agent-induced dehydration. Figures 2(b2) and 2(c2) are the corresponding OCT angiograms before and after FPT treatment, respectively. The blood vessels are isolated from the tissue bed. The big vessels mainly appear at the HD layer, as indicated by the bold arrows, and the small vessels above the HD layer come from the dermis, as indicated by the thin arrows. As shown in Fig. 2(c2), most of the dermal small vessels disappear after the FPT treatment, and the HD blood vessels present an improved visibility, most likely due to the decreased scattering attenuation in the dermis, which can be also observed in the projection view of the 3-D angiography in Figs. 2(b3) and 2(c3). The dermal vasculature can be observed before the FPT treatment in Fig. 2(b3), while the HD big vessels exhibit an improved contrast after the FPT treatment in Fig. 2(c3).

3.2 *Quantifications of Skin Optical Properties*

The skin surface can be identified in the OCT structural cross-sections. The outermost surface was flatted to align all the depth profiles. Then, the OCT depth profile was averaged along the lateral direction so as to reduce effects of the heterogenetic distribution of the cutaneous absorbers and scatters as much as possible. As shown in Fig. 3(a), the solid blue and dashed red curves correspond to the depth profiles before and after the FPT

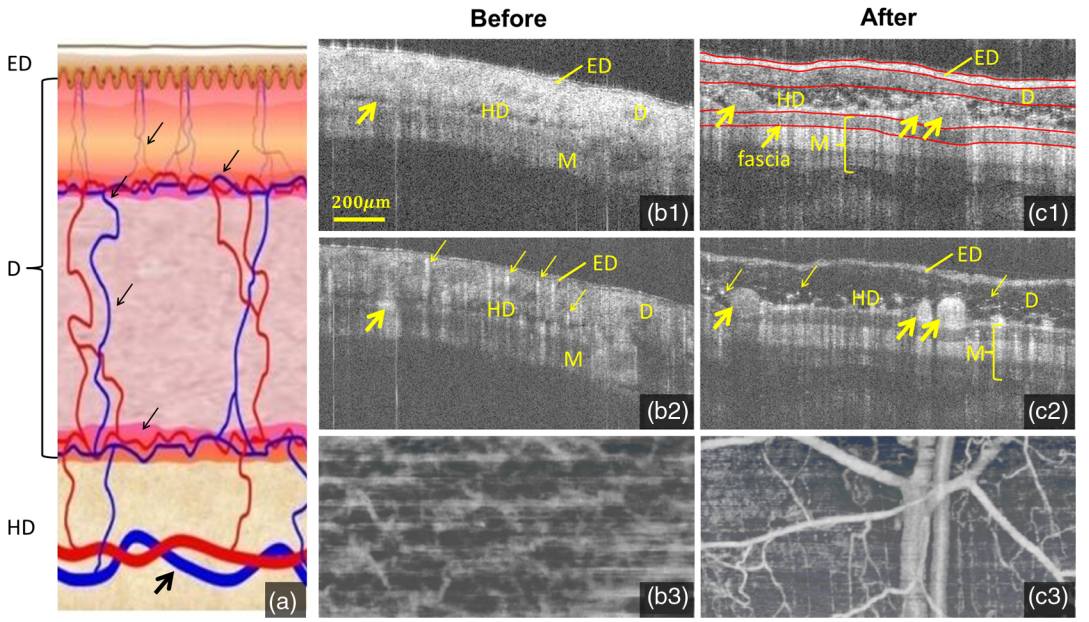

Fig. 2 Representative OCT structural and angiographic images of mouse dorsal skin *in vivo*, before (column b) and after (column c) FPT treatment, respectively. (a) Cross-sectional schematic of the layered skin. (b1) and (c1) Structural cross-sections. (b2) and (c2) Cross-sectional angiograms. (b3) and (c3) Projection view of 3-D angiography. ED, epidermis; D, dermis; HD, hypodermis; M, muscles. Thin arrows indicate small vessels. Bold arrows indicate big vessels.

treatment, respectively. After the FPT treatment, OCT intensity strength exhibits a decrease of ~25.6% in the D and HD layers, with an increase of ~42.5% in the M layer. The attenuation coefficient image was calculated according to Eq. (2); thereafter, the outermost surface was flattened and the depth-resolved attenuation coefficient was calculated by averaging the attenuation coefficient image along the lateral direction, as shown in Fig. 3(b). After the FPT treatment, the attenuation coefficients were lower: ~40.5% for the ED, D, and HD layers, and ~11.6% for the M layer.

As mentioned before, the relative changes in the refractive-index mismatching extent (m) between tissue components and extracellular fluid could be quantified using Eq. (3). As shown in Fig. 3(c), the solid blue line represents the relative changes in $(m-1)$ after FPT treatment, indicating an average decline of ~25.3% in the ED, D, and HD layers, and ~6.1% in the muscle layer, respectively. The dashed red line is the relative changes in Angio-OCT signal strength. Thereafter, we calculated the correlation between the relative changes in refractive-index mismatching $(m-1)$ and Angio-OCT signal strength using Eq. (5), and the results demonstrate that the correlation between the relative changes in refractive-index mismatching $(m-1)$ and Angio-OCT signal strength are about 90% and −55% for the superficial (ED + D + HD) layers and the deeper (M) layer, respectively. In addition, the permeability rate P is $\sim 5.83 \times 10^{-5}$ cm/s using Eq. (4).

3.3 *Blood Flow Dynamic Responses*

With a combination of optical clearing methods, Angio-OCT exhibits enhanced performance in imaging skin blood flow, allowing cutaneous hemodynamic analysis with high

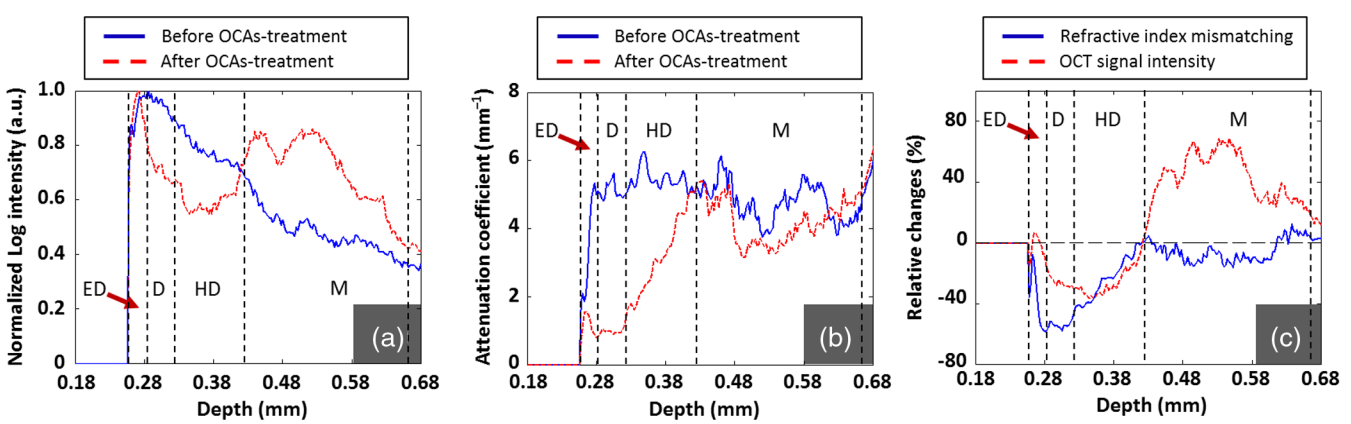

Fig. 3 (a) Normalized OCT depth profiles and (b) depth-resolved attenuation coefficients, before (solid blue curves) and after (dashed red curves) FPT treatment, respectively. (c) Relative changes in refractive-index mismatching extent (solid blue curve) and signal intensity (dashed red curve). The vertical dashed lines roughly indicate the skin layers.

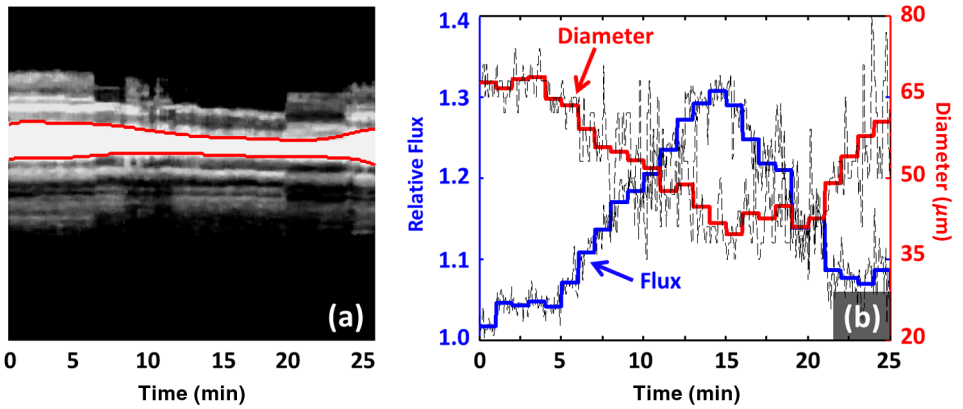

Fig. 4 Blood flow dynamic responses to vasoactive drug monitored by Angio-OCT. (a) The M-mode Angio-OCT image of the time-lapse blood flow dynamic responses (the fitted red curves enhance the visualization of response changes) and (b) the dynamic changes in vessel diameter and normalized blood flow flux.

spatiotemporal resolution and contrast. The vasoactive drug-induced changes of vascular diameter and flow flux are estimated over time. The flow flux is measured based on the signal strength of OCT angiograms and normalized with the baseline.

Figure 4(a) shows the M-mode Angio-OCT image of the time-lapse blood flow dynamic responses to vasoactive NE after FPT treatment, and the dynamic changes in vessel diameter, which were fitted with red curves, are obvious to see. Figure 4(b) reports the quantifications of the dynamic responses of vessel diameter and normalized blood flow. The baseline of vessel diameter is 64 μm. After NE injection, the diameter exhibits a gradual decrease of up to 32.8% at the time instant ~14 min, then returns to ~96% of the baseline in 25 min. Along with the dynamic change in diameter, the flow flux exhibits a gradual increase of up to ~30% at the time instant ~15 min, and then returns to ~105% of the baseline in 25 min.

4 Discussion and Conclusion

In this study, a newly developed OCA, FPT, is evaluated with Angio-OCT by quantifying skin optical property and blood flow imaging simultaneously. Angio-OCT offers depth-resolved information about the optical properties, enabling a further understanding of the OCA. Most likely due to the different levels of OCA-induced dehydration and refractive-index matching for each skin layer, there is an evident interface at the ED-D, D-HD, and HD-M junctions, as shown in the Angio-OCT structural cross-sections and depth profiles. As plotted in Figs. 3(b) and 3(c), the D layer presents the largest decrease in scattering coefficient and refractive-index mismatching, while the M layer corresponds to a minimal change.

Mainly due to the considerable decrease of attenuation in the superficial layers, more ballistic photons could penetrate into the deeper layers, leading to an improved imaging depth and blood flow contrast. As reported in this study, the application of skin OCAs leads to an improved imaging performance for the deeper tissues (refer to Fig. 2). The imaging performance improvement is most likely caused by the OCA-induced dehydration of skin, and the reduction of attenuation coefficient [refer to Fig. 3(b)] and refractive-index mismatching within the tissue [refer to Fig. 3(c)], as indicated by the high correlation between the relative changes in refractive-index mismatching $(m-1)$ and Angio-OCT signal strength [refer to Fig. 3(c)]. These were quite consistent with the conclusions by Ghosn et al.,[36] Zhong et al.,[37] Xu et al.,[38] and Wen et al.[39]

The permeability rate can also be measured by monitoring the OCT signal slope, the method developed in Ref. 21. The optical clearing rate is an important parameter for OCA evaluation. A fast permeability rate ensures a sufficient optical clearing efficacy within a short time, which is extremely significant for the *in vivo* study.

As discussed above, the FPT is an efficient agent for optical clearing, inducing a significant decrease in attenuation coefficient and refractive-index mismatching, and an improved penetration with a sufficient rate. Combined with optical clearing, Angio-OCT exhibits enhanced performance in imaging skin blood flow, allowing cutaneous hemodynamic analysis with satisfactory spatiotemporal resolution and contrast, and providing a powerful approach for studying skin microcirculation.

Acknowledgments

The authors acknowledge financial support from National Hi-Tech Research and Development Program of China (2015AA020515), National Natural Science Foundation of China (Grant Nos. 61475143, 11404285, 81171376, 91232710, 31571002, 61335003, 61327007, and 61275196), Zhejiang Provincial Natural Science Foundation of China (LY14F050007), Zhejiang Province Science and Technology Grant (2015C33108), Seed project of Wuhan National Laboratory for Optoelectronics, Science Fund for Creative Research Group (Grant No. 61421064), Fundamental Research Funds for the Central Universities (2014QNA5017), and Scientific Research Foundation for Returned Scholars, Ministry of Education of China.

References

1. S. M. Daly and M. J. Leahy, "'Go with the flow': a review of methods and advancements in blood flow imaging," *J. Biophotonics* **6**(3), 217–255 (2013).
2. J. Wang et al., "Evaluation of optical clearing with the combined liquid paraffin and glycerol mixture," *Biomed. Opt. Express* **2**(8), 2329–2338 (2011).
3. D. Zhu et al., "Recent progress in tissue optical clearing," *Laser Photonics Rev.* **7**(5), 732–757 (2013).
4. E. A. Genina, A. N. Bashkatov, and V. V. Tuchin, "Tissue optical immersion clearing," *Expert Rev. Med. Devices* **7**(6), 825–842 (2010).

5. J. Wang, R. Shi, and D. Zhu, "Switchable skin window induced by optical clearing method for dermal blood flow imaging," *J. Biomed. Opt.* **18**(6), 061209 (2013).
6. J. Wang et al., "Review: tissue optical clearing window for blood flow monitoring," *IEEE J. Sel. Top. Quantum* **20**(2), 680111 (2014).
7. E. A. Genina et al., "Optical coherence tomography monitoring of enhanced skin optical clearing in rats in vivo," *J. Biomed. Opt.* **19**(2), 021109 (2014).
8. R. K. Wang et al., "Concurrent enhancement of imaging depth and contrast for optical coherence tomography by hyperosmotic agents," *J. Opt. Soc. Am. B* **18**(7), 948–953 (2001).
9. Y. Liu et al., "Optical clearing agents improve photoacoustic imaging in the optical diffusive regime," *Opt. Lett.* **38**(20), 4236–4239 (2013).
10. Y. Zhou, J. Yao, and L. H. V. Wang, "Optical clearing aided photoacoustic microscopy with enhanced resolution and imaging depth," *Opt. Lett.* **38**(14), 2592–2595 (2013).
11. R. Dickie et al., "Three-dimensional visualization of microvessel architecture of whole-mount tissue by confocal microscopy," *Microvasc. Res.* **72**(1–2), 20–26 (2006).
12. R. Samatham, K. G. Phillips, and S. L. Jacques, "Assessment of optical clearing agents using reflectance-mode confocal scanning laser microscopy," *J. Innovative Opt. Health Sci.* **3**(3), 183–188 (2010).
13. R. Cicchi and F. S. Pavone, "Contrast and depth enhancement in two-photon microscopy of human skin ex vivo by use of optical clearing agents," *Opt. Express* **13**(7), 2337–2344 (2005).
14. A. Erturk et al., "Three-dimensional imaging of solvent-cleared organs using 3DISCO," *Nat. Protoc.* **7**(11), 1983–1995 (2012).
15. Y. Ding et al., "Signal and depth enhancement for in vivo flow cytometer measurement of ear skin by optical clearing agents," *Biomed. Opt. Express* **4**(11), 2518–2526 (2013).
16. J. Wang et al., "Sugars induced skin optical clearing from molecular dynamics simulation to experimental demonstration," *IEEE J. Sel. Top. Quantum* **20**(2), 7101107 (2014).
17. S. A. Prahl, M. J. C. van Gemert, and A. J. Welch, "Determining the optical properties of turbid media by using the adding-doubling method," *Appl. Opt.* **32**(4), 559–568 (1993).
18. X. Zhong, X. Wen, and D. Zhu, "Lookup-table-based inverse model for human skin reflectance spectroscopy: two-layered Monte Carlo simulations and experiments," *Opt. Express* **22**(2), 1852–1864 (2014).
19. Z. Deng et al., "Viscous optical clearing agent for in vivo optical imaging," *J. Biomed. Opt.* **19**(7), 076019 (2014).
20. A. F. Pena et al., "Monitoring of interaction of low-frequency electric field with biological tissues upon optical clearing with optical coherence tomography," *J. Biomed. Opt.* **19**(8), 086002 (2014).
21. K. V. Larin et al., "Optical clearing for OCT image enhancement and in-depth monitoring of molecular diffusion," *IEEE J. Sel. Top. Quantum* **18**(3), 1244–1259 (2012).
22. J. Senarathna et al., "Laser speckle contrast imaging theory, instrumentation and applications," *IEEE Rev. Biomed. Eng.* **6**, 99–110 (2013).
23. D. A. Boas and A. K. Dunn, "Laser speckle contrast imaging in biomedical optics," *J. Biomed. Opt.* **15**(1), 011109 (2010).
24. M. Draijer et al., "Review of laser speckle contrast techniques for visualizing tissue perfusion," *Laser Med. Sci.* **24**(4), 639–651 (2009).
25. R. Shi et al., "Accessing to arteriovenous blood flow dynamics response using combined laser speckle contrast imaging and skin optical clearing," *Biomed. Opt. Express* **6**(6), 1977–1989 (2015).
26. Y. Zhang et al., "Time-domain interpolation for Fourier-domain optical coherence tomography," *Opt. Lett.* **34**(12), 1849–1851 (2009).
27. Y. Cheng et al., "Statistical analysis of motion contrast in optical coherence tomography angiography," *J. Biomed. Opt.* **20**(11), 116004 (2015).
28. M. Roustit and J. L. Cracowski, "Assessment of endothelial and neurovascular function in human skin microcirculation," *Trends Pharmacol. Sci.* **34**(7), 373–384 (2013).
29. J. Enfield, E. Jonathan, and M. Leahy, "In vivo imaging of the microcirculation of the volar forearm using correlation mapping optical coherence tomography (cmOCT)," *Biomed. Opt. Express* **2**(5), 1184–1193 (2011).
30. Y. M. Liew et al., "In vivo assessment of human burn scars through automated quantification of vascularity using optical coherence tomography," *J. Biomed. Opt.* **18**(6), 061213 (2013).
31. W. J. Choi et al., "Improved microcirculation imaging of human skin in vivo using optical microangiography with a correlation mapping mask," *J. Biomed. Opt.* **19**(3), 036010 (2014).
32. L. Guo et al., "Improved motion contrast and processing efficiency in OCT angiography using complex-correlation algorithm," *J. Optics-UK* **18**(2), 025301 (2016).
33. R. He, "Effects of optical clearing agents on noninvasive blood glucose monitoring with optical coherence tomography: a pilot study," *J. Biomed. Opt.* **17**(10), 101513 (2012).
34. K. A. Vermeer et al., "Depth-resolved model-based reconstruction of attenuation coefficients in optical coherence tomography," *Biomed. Opt. Express* **5**(1), 322–337 (2014).
35. V. V. Tuchin, *Optical Clearing of Tissues and Blood*, pp. 1–129, SPIE Press, Bellingham (2005).
36. M. G. Ghosn et al., "Monitoring of glucose permeability in monkey skin in vivo using optical coherence tomography," *J. Biophotonics* **3**(1–2), 25–33 (2010).
37. H. Zhong et al., "Synergistic effect of ultrasound and thiazone-PEG 400 on human skin optical clearing in vivo," *Photochem. Photobiol.* **86**(3), 732–737 (2010).
38. X. Xu, Q. Zhu, and C. Sun, "Assessment of the effects of ultrasound-mediated alcohols on skin optical clearing," *J. Biomed. Opt.* **14**(3), 030442 (2009).
39. X. Wen et al., "Enhanced optical clearing of skin in vivo and optical coherence tomography in-depth imaging," *J. Biomed. Opt.* **17**(6), 066022 (2012).

Biographies for the authors are not available.